

Unravelling the multiscale surface mechanics of soft solids

Nicolas Bain,^{1,2,*} Lawrence A. Wilen,³ Dominic Gerber,² Mengjie Zu,⁴ Carl P. Goodrich,⁴ Senthilkumar Duraivel,⁵ Kaarthik Varma,⁵ Harsha Koganti,⁵ Robert W. Style,² and Eric R. Dufresne⁵

¹*University of Lyon, Université Claude Bernard Lyon 1, CNRS, Institut Lumière Matière, F-69622, Villeurbanne, France.*

²*Department of Materials, ETH Zürich, 8093 Zürich, Switzerland.*

³*Yale University, New Haven, Connecticut 06520, USA.*

⁴*Institute of Science and Technology Austria (ISTA), Am Campus 1, 3400 Klosterneuburg, Austria.*

⁵*Department of Materials Science and Engineering, Department of Physics, Cornell University, Ithaca, NY, USA.*

(Dated: October 15, 2024)

The softer a material is, the more its mechanics are sensitive to interfaces. In soft gels, an elastic polymeric network is filled with free-flowing molecules. In theory, either of these components could dominate the material interfacial properties. In practice, current measurements cannot distinguish between the two, nor can they rule out material inhomogeneities, which could modulate the apparent properties of the interfaces. Here, we introduce an experimental approach that elucidates the interfacial mechanics of soft solids. Coupling quantum dots, controlled deformations, and precise confocal measurements, we fully separate the material inhomogeneities of a silicone gel from its true interfacial properties. We quantify a gradient in bulk elastic properties near the surface, with a characteristic length scale of about 20 μm . In addition, we observe a surface excess elasticity, whose associated gradient is unresolvable with light microscopy. The composition of the external medium has a strong affect on the observed value of the surface elasticity. Thus, we conclude that the surface elasticity of this silicone network is an interfacial property.

INTRODUCTION

Whether they come from an engineered external layer or an intrinsic structure, surface properties are essential in determining and tuning materials responses. An appropriate surface coating can render a body conductive for scanning electron microscopy [1], stabilize the cathode–electrolyte interface in Li-ion batteries [2], or prevent water from penetrating a fibrous network [3]. In turn, interfacial excess free energy [4] is key to the efficiency of water harvesting [5], the strength of pressure-sensitive adhesives [6], and the coarsening of liquid-liquid phase separated systems [7].

In soft polymeric materials, surface mechanical properties determine wetting, friction, and adhesion performances, up to an *elastocapillary length* equal to the ratio of surface tension and elastic modulus of the bulk [8, 9]. Although there is a wide consensus on the importance of surface effects in such materials, their fundamental nature is a controversial topic. In polymer gels, in particular, the cohabitation of a crosslinked network with free-flowing molecules obfuscates the origins of an interfacial energy. Is it defined by the chemical composition, or by the larger scale organization of the network? The dominant approach to tackle this question has been to look at variations of surface tension under stretch [10–14]. Simply stated, if surface tension does not change when the surface is stretched, it is dominated by chemical composition. If it does, the elastic network necessarily

plays a role. Measuring the stretch-dependence of surface tension, so far, has been challenging. It requires mechanically probing a soft material at length scales where the surface plays a role, in a configuration where we can suppress the bulk response and isolate surface effects. Material and geometric nonlinearities can complicate the separation of bulk and interfacial properties [10, 11, 15–17]. Yet, even when accounting for these effects [14], we assume that the impact of the interface is localized to an unresolved layer, much thinner than any other length scale in the mechanical test. Surface-induced modulation of bulk material properties, for example on the scale of the elastocapillary length, would severely impact the interpretation of any experiment assuming a homogeneous bulk response.

In this paper, we independently assess bulk and surface mechanical properties of soft polymeric materials, based on local measurements in the small deformation regime. We unveil a multiscale impact of the interface on a material’s mechanical response. First, we find a two-fold drop of the shear modulus, within 20 μm of the surface. Second, we find a surface excess elastic response, at unresolved scales, that depends on the composition of the surrounding medium. Generally, these results demonstrate how the multi-scale structure of a polymer gel can influence its mechanical response. Specifically, it shows that polymer gels have a surface elasticity, which depends, like other classical interfacial properties, on the composition of the surrounding medium.

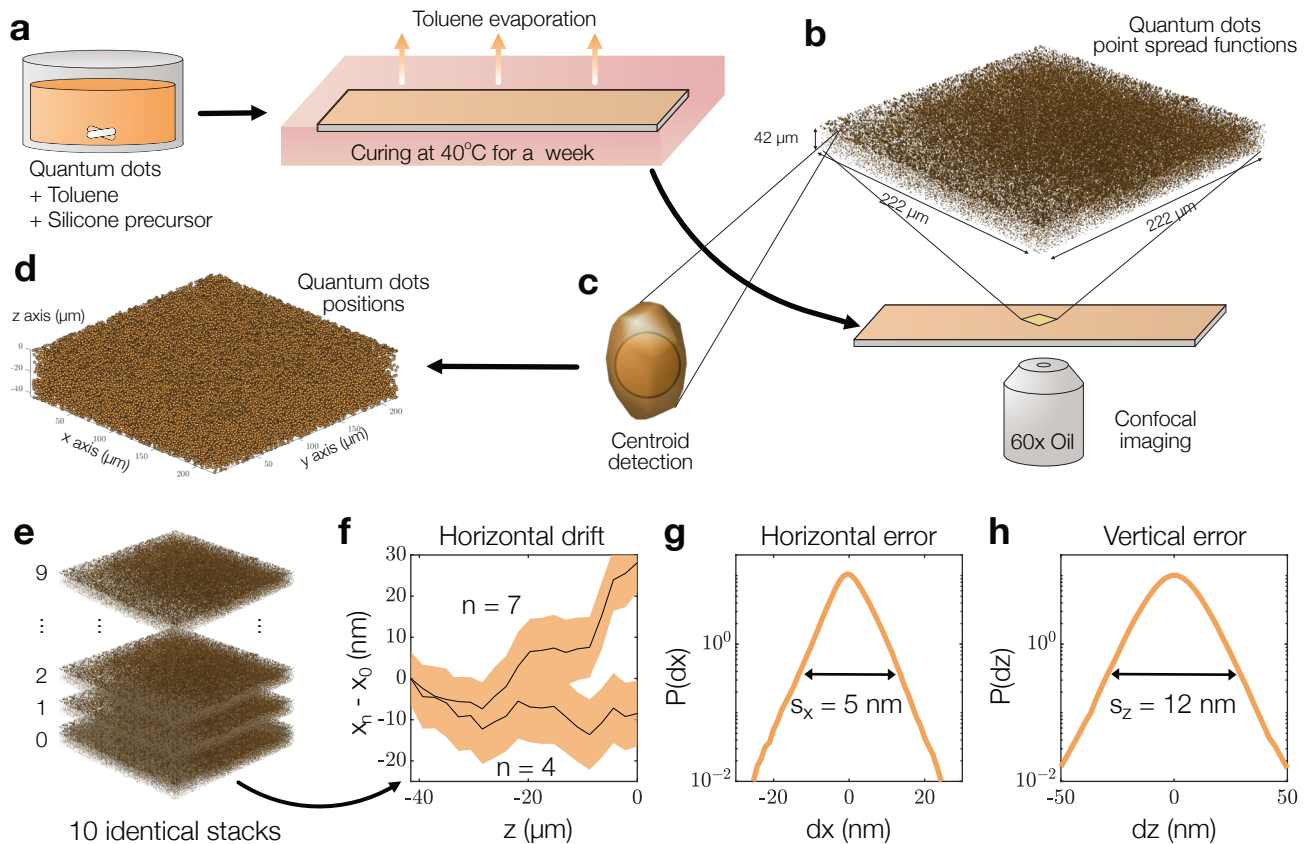


Fig. 1. (a) Schematic of the quantum dots incorporation process. First, we mix quantum dots dispersed in toluene with the soft silicone precursor. We then put the mix onto a coverslip, quickly evaporate the excess toluene, and cure the sample at 40°C for a week. (b) Three-dimensional confocal reconstruction of the quantum dots point spread functions. (c) We determine the tridimensional position of each quantum dot by fitting the associated point spread function with an ellipsoid. (d) Three-dimensional measured positions of all quantum dots in a confocal stack. (e) To determine the experimental noise, we image the same location ten consecutive times. (f) Difference in the measured x positions between stacks 7 and 0, and between stacks 4 and 0. (g) Probability distribution function for the error on the horizontal detection. (h) Probability distribution function for the error on the vertical detection. Sketches not to scale.

QUANTUM DOTS HIGH PRECISION 3D LOCATION AND TRACKING

We show the process to seed a soft PDMS with quantum dots in Fig. 1a. First, the silicone precursor is poured into a solution of toluene-dispersed quantum dots. The mix is then deposited on a coverslip, spin-coated, degassed to remove the excess toluene, and cured at 40°C for a week (see Methods for details). Just before imaging the sample, we cover it with a layer of 100 nm fluorescent beads following usual protocols [10, 11, 18, 19]. Under confocal microscopy, the fluorescence of the quantum dots reveals their positions, which we capture in 3D image stacks (Fig. 1b). We fit each point spread function with an ellipsoid to obtain the center of mass of the tracers (Fig. 1c,d). Except for a small depletion-accumulation zone near the bottom and top surfaces, the tracers are homogeneously dispersed within the soft solid. With a mean density of $0.035 \mu\text{m}^{-3}$, the 5 nm quantum dots are on average $3 \mu\text{m}$ away from each other and occupy $10^{-8}\%$ of the total volume, too little to alter its

mechanical properties. On the top surface, the 100 nm beads have a similar inter-particle spacing and occupy $3 \times 10^{-4}\%$ of the total area, also too small to matter.

The fundamental quantity to measure material deformations is the gradient of displacements $\nabla\mathbf{u}$. We verify how precisely we measure it by taking advantage of the static nature of our setup. We image the same immobile location ten consecutive times, and compare the subsequently obtained positions (Fig. 1e). We link the tracers from one set to the next with the tracker described in [20], and only keep the ones found in all ten stacks. With this procedure, we identify two sources of noise. First, a small z -dependent shift between each stack (Fig. 1f), which we attribute to a slow drift of the microscope stage [21]. If the stage moves while we acquire a confocal stack, every slice of the stack will be shifted compared to the same slice of a previously acquired stack. The largest shift being of 30nm over the $40\mu\text{m}$ thick sample, it will result in a systematic error in the displacement vertical gradients $\partial u/\partial z$ of the order of 0.1%. Second, an uncertainty in the evaluation of the point spread functions center of mass

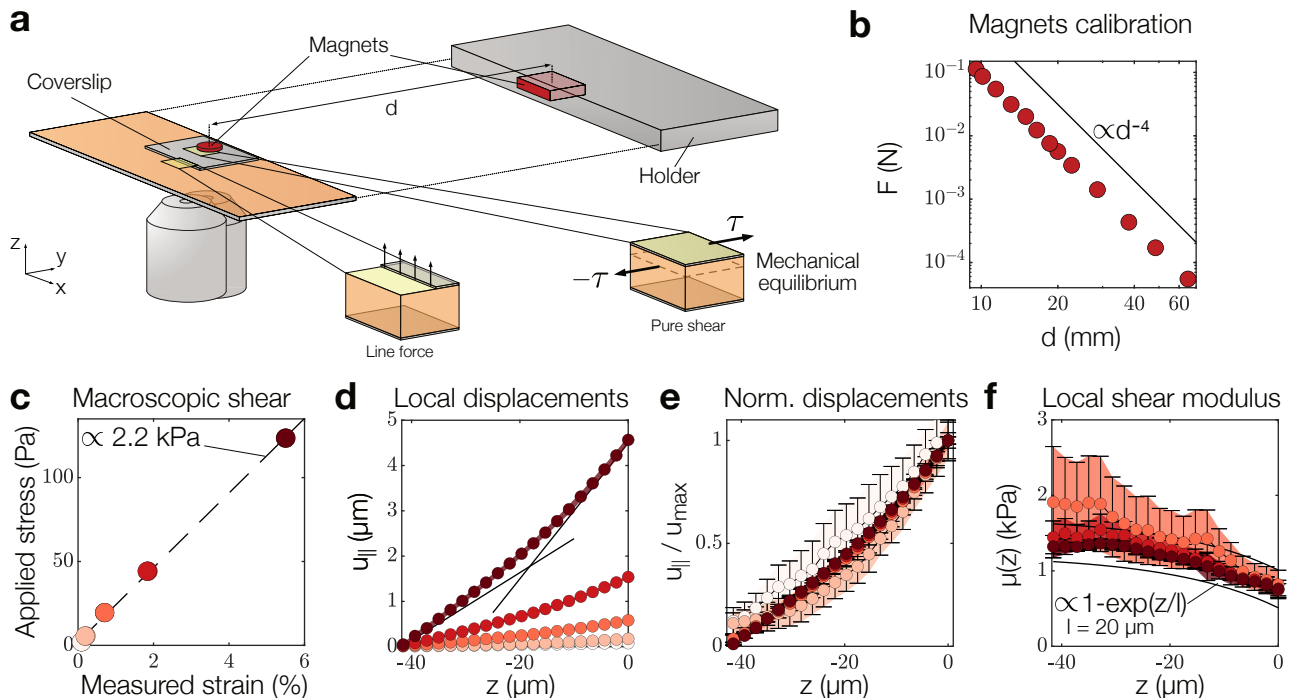


Fig. 2. (a) Schematic of the bulk elasticity measurement setup. We deposit a small coverslip with a magnet attached atop the soft solid. We place another magnet into a vertically-aligner holder to constrain the soft solid in pure shear below the small coverslip. There, mechanical equilibrium prescribes that the shear stress τ is applied uniformly throughout the sample. At the edge of the coverslip, the interfacial tension acts as a line force. Sketches not to scale. (b) Intermagnet force as a function of intermagnet distance. (c) Macroscopic strain-stress relationship, together with the line $\tau = 2\mu\epsilon$ with $\mu = 1.1\text{kPa}$. (d) Horizontal displacements u_{\parallel} as a function of the vertical position z . (e) Horizontal displacements normalized by the maximal horizontal displacement u_{max} . (f) Local shear modulus $\mu(z)$ as a function of the vertical position z . Plots (c) to (f): each color codes for an imposed macroscopic stress. Plots (d), (e) (resp. (f)) are computed from the horizontal displacements (resp. shear strain $(\partial u_{\parallel}/\partial z)/2$) averaged over regularly spaced slabs of thickness $2.2\ \mu\text{m}$. The size of the errorbars equates twice the associated standard deviations.

(Fig. 1c). After correcting for the stage motion, the probability distribution functions of the tracer location error follow a distribution with exponential tails (Fig. 1g,h), with a standard error of $\delta_x = 5\ \text{nm}$ in the (x, y) directions and of $\delta_z = 12\ \text{nm}$ in the z direction, much smaller than the voxel dimensions $(100 \times 100 \times 270)\text{nm}^3$. This leads to a random error in the displacement gradients of $\delta_{\delta_{x,z}}/L$, with L the distance over which the gradient is calculated. With a mean tracer-to-tracer distance of $3\ \mu\text{m}$, we estimate that in the absence of spatial averaging the error on the horizontal gradients are of 0.2%, and the error on the vertical gradients of 0.4%.

In the following, we measure local displacements by tracking the tracers between a set of initial and final configurations. We keep only the ones found in all the confocal stacks, and evaluate the displacement gradient $\nabla\mathbf{u}$ at each tracer location with a local polyharmonic spline interpolation scheme [22] (see Methods for details).

BULK ELASTICITY IS NOT HOMOGENEOUS

We elucidate the mechanical properties of the soft PDMS with a pure shear experiment. We deposit a $1 \times 1\ \text{cm}^2$ coverslip on top of the soft PDMS, confining it between two parallel planes. We then tape a small flat

cylindrical magnet on the top coverslip, and mount a larger magnet on the sample holder, in a 3D-printed mobile part calibrated such that the two magnets are vertically aligned (Fig. 2a). By moving the mobile part, we can approach the two magnets to increase their attraction force (Fig. 2b). While the large magnet is stuck in its holder, the small one is attached to the soft solid. It then responds to the magnetic field by moving towards the large magnet, deforming the material underneath. We record the induced displacement at various inter-magnet distances and, after calibration of the magnets force-distance relation (see Methods for more details), report a linear macroscopic strain-stress relationship (Fig. 2c). With this macroscopic measurement, we estimate that the soft PDMS has a shear modulus of 1.1 kPa, consistent with previous experiments on this material [14].

We now investigate the local mechanical response. We inspect how the tracers inside the material are displaced by the horizontal motion of the top coverslip (Fig. 2d). If the material were homogeneous, the horizontal displacements u_{\parallel} would linearly decay from the moving top surface to the fixed bottom one. Instead, we observe that

the horizontal motion of the tracers decay non-linearly, faster close to the top surface (Fig. 2d). This behavior is not limited to the larger imposed deformations. It is also present for strains smaller than 2%, deep inside the linear regime of soft PDMS [14], and all the displacement profiles collapse when normalized by the maximal displacement (Fig. 2e).

To rationalize this behavior, we proceed to a force balance. We mentally isolate a slab of PDMS, which includes its top surface (Fig. 2a). On the top surface, the coverslip exerts a horizontal force per unit area τ . We call it the shear stress. For the slab to be at mechanical equilibrium, the PDMS below it has to exert an opposite force per unit area of amplitude τ . This being true independently for every slab, independently of its thickness, the shear stress inside the material is homogeneous and equal to τ . The shear strain, $\epsilon = (\partial u_{\parallel} / \partial z) / 2$, is however not homogeneous but follows a vertical gradient (Fig. 2d). As a consequence, the shear modulus $\mu = \tau / 2\epsilon$ also varies with the distance from the top surface (Fig. 2f). This variation extends over the whole thickness, and the shear modulus doubles between the top and bottom surfaces. Surprisingly, this gradient of mechanical properties resembles surface layers previously reported in hydrogels due to oxygen inhibition of free-radical polymerization [23]. Such behavior has however never been reported in silicone materials. Interestingly, the good agreement between the shear modulus profile and an exponential decay, with decay length $l = 20 \mu\text{m}$ (Fig. 2f), is consistent with a reaction-diffusion model [24, 25].

SURFACE ELASTICITY IS AN INTERFACIAL PROPERTY

We take advantage of the deformations at the wetting ridge of sessile drop (Fig. 3a) and at the edge of the coverslip (Fig. 2a) to probe the surface elastic response. We will discuss the former in details here, and the latter in Supplementary Information. It is well established that, for soft solids, a force as minute as a pulling contact line induces large deformations [19]. Simply put, a dimensional analysis predicts that a contact line, with a surface tension Γ , will deform a solid of stiffness μ over length scales comparable to the elastocapillary length $L_{ec} = \Gamma / \mu$. The challenge here, to obtain the displacement gradient $\nabla \mathbf{u}$, is to image the same location before and after the droplet deforms it. To this end, we first deposit a small drop of glycerol on the sample of soft PDMS. We then image a line of five overlapping consecutive stacks at a distance from the drop, where the material is undeformed, covering a distance of one millimeter (see Methods for details). These constitute a pool of potential reference states. Next, we expand the small droplet with extra glycerol, until its contact line reaches the first imaged undeformed state. We let the droplet equilibrate overnight, and the location where the contact

line stopped indicates which reference states to use. We eventually image ten times both the inner and the outer sides of the contact line (Fig. 3a).

We superimpose the radially-collapsed tracer positions on both sides of the contact line in Fig. 3b. Similarly to previous work [19], we observe a wetting ridge with a well-defined opening angle. In contrast, however, the wetting ridge is rounded off and does not present a sharp tip. This apparent contradiction can be explained by the time waited before imaging the deformed state. In [19], the authors image the wetting ridge immediately after depositing a droplet. Here, we do so after several hours. During that time, although the glycerol does not swell the PDMS [26], the high stresses at the tip of the ridge expel some of the free chains, and the geometry relaxes poroelastically to its equilibrium shape [27–30]. Yet, the measured opening angle of 110° is consistent with the one observed at that scale in [19] (Fig. 3c), and we conclude that the interfacial tensions on both sides of the ridge are of the order of 30 mN/m here as well.

We now turn to the response of the surface to external deformations. As we just saw, the vicinity of the wedding ridges brings about many complications, among which large, and poroelastic deformations. We will then focus on the small deformation regime, away from the contact line. In addition, we revealed in the previous part that the material was inhomogeneous, and presented a vertical gradient of elastic properties. We therefore cannot benefit from the abundant literature on traction force microscopy models that rely on the homogeneity assumption [31–33]. Instead, we need to estimate stresses and strains locally from the measured displacement gradient $\nabla \mathbf{u}$. We classically define $\mathbf{E} = (\mathbf{F}^T \mathbf{F} - \mathbf{I}) / 2$ the Green strain, with $\mathbf{F} = \mathbf{I} + \nabla \mathbf{u}$. To estimate the surface deformations, we take advantage of the radial symmetry of the system. We define \mathbf{t} the unit vector tangent to the surface pointing in the radial direction, \mathbf{n} the unit vector normal to the surface, and $\mathbf{p} = \mathbf{n} \times \mathbf{t}$ the unit vector in the hoop direction (Fig. 3b, see Methods for details). We then evaluate the amount by which the surface is stretched by projecting the strain of the surface points along the different spatial directions. The surface strain in the radial direction is equal to $E_t = \mathbf{t} \cdot \mathbf{E} \cdot \mathbf{t}$, shown in (Fig. 3d), and in the hoop direction to $E_p = \mathbf{p} \cdot \mathbf{E} \cdot \mathbf{p}$, shown in (Fig. 3e). As expected, the surface is not stretched in the hoop direction. Along the radial direction, however, it grows from 0 in the far-field to 2% over $100 \mu\text{m}$ on both sides of the wetting ridge, before sharply decreasing and blowing up close to the contact line. From now on, we will focus on the small-deformation regime and only consider the area from the far field and up to the 2% deformation point (Fig. 3c).

Between both sides of each interface, the stresses differ. On the one hand, the normal stress σ_{nn} increases by the Laplace pressure $\kappa \Gamma$, where Γ is the interfacial tension and κ the local curvature. On the other hand, the

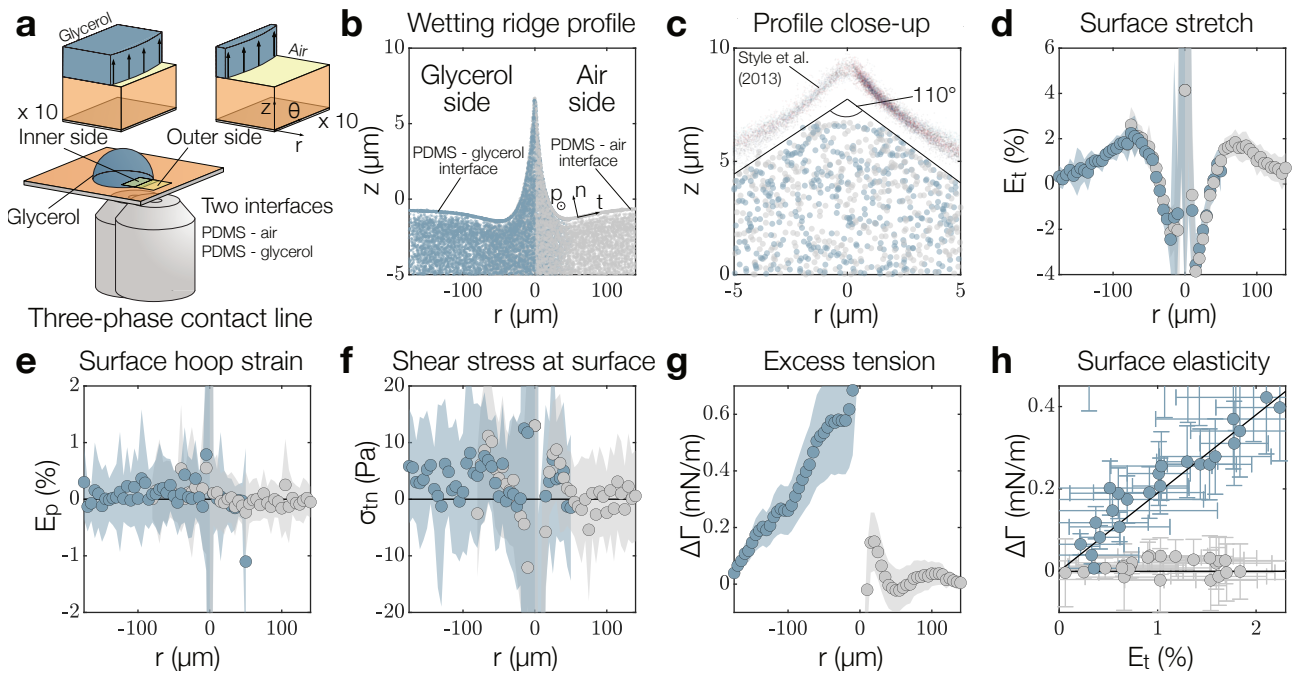


Fig. 3. (a) Sketch of the three-phase contact line confocal imaging. We acquire 10 confocal stacks of both the inner and the outer side of the contact line. Sketches not to scale. (b) and (c) Radially-collapsed quantum dots positions on both sides of the wetting ridge. t , n , and p represent the unit vectors respectively tangent, normal to the surface, and in the hoop direction. The cloud of points above the solid lines in (c) corresponds to the wetting ridge data presented in [19], to scale. (d), (e), (f), and (g): stretch E_t , hoop strain E_p , shear stress σ_{tn} , and excess interfacial tension $\Delta\Upsilon$ of the surface tracers, as a function of the radial position r . (h) Excess interfacial tension $\Delta\Upsilon$ as a function of the surface stretch E_t . The solid lines correspond $\Delta\Upsilon = \Lambda E_t$, with $\Lambda = 0$, and $\Lambda = 19$ mN/m. In (b) to (h), the data points corresponding to the tracers below the glycerol droplets are depicted in blue, and the other ones in gray. In (d) to (h), for each detected tracer, the strains, stresses, and excess interfacial tension are computed from the displacements between the initial configuration and each of the ten imaged final configurations. The circles correspond to the average over the ten datasets, and the width of the shaded area and errorbars equate twice the associated standard deviation.

tangential stress σ_{tn} increases by the gradient of surface tension $\partial\Gamma/\partial s$, where s is the curvilinear abscissa [16]. Soft PDMS being incompressible, the normal stress can only be determined up to a pressure term [34]. The tangential stress, however, can be determined exactly. To do so, we evaluate the stress tensor at the location of the surface tracers, $\boldsymbol{\sigma} = 2\mu\mathbf{E}$, and project it on the normal and tangential directions $\sigma_{tn} = \mathbf{t} \cdot \boldsymbol{\sigma} \cdot \mathbf{n}$ (Fig. 3f). We then calculate the interfacial excess tension $\Delta\Gamma = \int \sigma_{tn} ds$ on both sides of the contact line by integrating the tangential stress from the far field (Fig. 3g). At the PDMS-air interface, the tangential stress is nearly zero and the excess tension remains null (Fig. 3f,g). In stark contrast, the tangential stress is strictly positive on the PDMS-glycerol interface, and the excess tension increases by 0.5 mN/m along the stretched interface (Fig. 3f,g). More precisely, the PDMS-air interfacial tension remains constant under stretch while the PDMS-glycerol tension increases linearly with stretch $\Delta\Gamma = \Lambda E_{tt}$ with a surface modulus of 19 mN/m (Fig. 3h).

The difference in surface elasticity on both sides of the contact line is statistically significant within a single measurement and was observed consistently across on five different instances. We considered a few artifacts thought

might lead to differences in the surface response on the two sides of the interface. First, we verified that the shear stress on the glycerol side could not be explained by hydrodynamic flow. Second, we localized changes to material properties due to the dissolution of glycerol into polymer network, which was found to be less than one part in 10^4 parts in equilibrium swelling. As a consequence, we conclude that surface elasticity is a proper interfacial property, depending on the composition of the material, as well as the surrounding medium.

CONCLUSION

We developed a method, based on nanotracers, controlled deformations, confocal imaging, and high-precision tracking, to locally measure bulk and surface properties of soft polymeric materials. We applied it to a soft silicone gel in the small deformation regime, and revealed two features that could not have been inferred in previous non-local [14] or large deformations [10] measurements. A vertical gradient of the bulk elastic properties, which extends over tens of microns, and an environment-dependent surface elasticity, which arises from molecular arrangements over an unresolved-thin surface layer.

These results suggest a hierarchy of length scales associated with the interface, and invite us to think carefully about the definition of surface properties. Interfacial properties, as defined by Gibbs, emerge from variation of some bulk property over an unresolved lengthscale near an interface [4]. This definition does not assume that surface excess properties emerge at the smallest structural scale, just that they are unresolved. Interfacial properties can therefore arise from excess quantities spanning over molecular or supramolecular scales. In a polymer network, interfacial properties could be defined at the monomer scale, the mesh scale, or over larger length scales defined through the creation of a heterogeneous mesh. In these experiments, the depth dependent modulus, varying over tens of microns, is suggestive of a heterogeneous mesh. Strain dependent interfacial tension is inconsistent with models of ideal polymer networks, whose interfacial properties have been shown in numerical simulations to be independent of the degree of crosslinking, thanks to the extreme flexibility of the chains [35]. Our observation of medium-dependent surface elasticity suggests that the mesh-scale structure of the network plays an essential role. While the microscopic mechanism of surface elasticity in these experiments remains undefined, we expect that it is related to the preferential localization of relatively polar moieties to the interface that remain tethered to cross-linked network. In that way, we hypothesize that it is related to adaptive wetting phenomena that have recently been observed in polymer gels [36].

AUTHOR CONTRIBUTIONS:

N.B. and E.R.D. conceived the project and designed the experiments. L.A.W. designed and made the magnetic holder, and performed the magnet calibration curves. S.D., K.V., and H.K performed the swelling and the NMR measurements. N.B. performed the experiments, with input from D.G. N.B. analyzed the experiments. N.B. and E.R.D. interpreted the experiments, with input from M.Z, C.P.G, and R.W.S. N.B. wrote the paper with inputs from all authors. E.R.D. supervised the project.

ACKNOWLEDGEMENTS:

The authors thank Stefanie Heyden, Thomas Salez, and Francesco Picella for useful discussions.

* nicolas.bain@cnrs.fr

- [1] A. Boyde and S. Reid, *Nature* **302** (1983).
- [2] H. Yu, Y. Cao, L. Chen, Y. Hu, X. Duan, S. Dai, C. Li, and H. Jiang, *Nature Communications* **12**, 4564 (2021).
- [3] D. L. Schmidt, C. E. Coburn, B. M. DeKoven, G. E. Potter, G. F. Meyers, and D. A. Fischer, *Nature* **368**, 39 (1994).
- [4] J. W. Gibbs, *American Journal of Science* **3**, 441 (1878).
- [5] H. Lu, W. Shi, Y. Guo, W. Guan, C. Lei, and G. Yu, *Advanced Materials* **34**, 2110079 (2022).
- [6] C. Creton, *MRS bulletin* **28**, 434 (2003).
- [7] J. W. Cahn, *Acta metallurgica* **9**, 795 (1961).
- [8] R. W. Style, A. Jagota, C.-Y. Hui, and E. R. Dufresne, *Annual Review of Condensed Matter Physics* **8**, 99 (2017).
- [9] B. Andreotti and J. H. Snoeijer, *Annual review of fluid mechanics* **52**, 285 (2020).
- [10] Q. Xu, K. E. Jensen, R. Boltyanskiy, R. Sarfati, R. W. Style, and E. R. Dufresne, *Nature communications* **8**, 1 (2017).
- [11] Q. Xu, R. W. Style, and E. R. Dufresne, *Soft Matter* **14**, 916 (2018).
- [12] R. D. Schulman, M. Trejo, T. Salez, E. Raphaël, and K. Dalnoki-Veress, *Nature communications* **9**, 1 (2018).
- [13] A. Carbonaro, K.-N. Chagua-Encarnacion, C.-A. Charles, T. Phou, C. Liguore, S. Mora, and D. Truzzolillo, *Soft Matter* **16**, 8412 (2020).
- [14] N. Bain, A. Jagota, K. Smith-Mannschott, S. Heyden, R. W. Style, and E. R. Dufresne, *Physical Review Letters* **127**, 208001 (2021).
- [15] R. Masurel, M. Roché, L. Limat, I. Ionescu, and J. Derieux, *Physical review letters* **122**, 248004 (2019).
- [16] A. Pandey, B. Andreotti, S. Karpitschka, G. Van Zwieten, E. Van Brummelen, and J. Snoeijer, *Physical Review X* **10**, 031067 (2020).
- [17] S. Heyden and N. Bain, *Soft Matter* **20**, 5592 (2024).
- [18] E. R. Jerison, Y. Xu, L. A. Wilen, and E. R. Dufresne, *Physical review letters* **106**, 186103 (2011).
- [19] R. W. Style, R. Boltyanskiy, Y. Che, J. Wettlaufer, L. A. Wilen, and E. R. Dufresne, *Physical review letters* **110**, 066103 (2013).
- [20] J. Y. Kim, S. Heyden, D. Gerber, N. Bain, E. R. Dufresne, and R. W. Style, *Phys. Rev. X* **11**, 031004 (2021).
- [21] J. Jonkman, C. M. Brown, G. D. Wright, K. I. Anderson, and A. J. North, *Nature protocols* **15**, 1585 (2020).
- [22] A. Iske, *Multiresolution methods in scattered data modelling*, Vol. 37 (Springer Science & Business Media, 2004).
- [23] J. Mandal, K. Zhang, N. D. Spencer, *et al.*, *Soft Matter* **17**, 6394 (2021).
- [24] A. M. Turing, *Bulletin of mathematical biology* **52**, 153 (1990).
- [25] S. Kondo and T. Miura, *science* **329**, 1616 (2010).
- [26] J. N. Lee, C. Park, and G. M. Whitesides, *Analytical chemistry* **75**, 6544 (2003).
- [27] Y. Hu and Z. Suo, *Acta Mechanica Solida Sinica* **25**, 441 (2012).
- [28] Q. Xu, L. A. Wilen, K. E. Jensen, R. W. Style, and E. R. Dufresne, *Physical Review Letters* **125**, 238002 (2020).
- [29] K. E. Jensen, R. Sarfati, R. W. Style, R. Boltyanskiy, A. Chakrabarti, M. K. Chaudhury, and E. R. Dufresne, *Proceedings of the National Academy of Sciences* **112**, 14490 (2015).
- [30] M. M. Flapper, A. Pandey, M. Essink, E. Van Brummelen, S. Karpitschka, and J. Snoeijer, *Physical review letters* **130**, 228201 (2023).
- [31] R. W. Style, R. Boltyanskiy, G. K. German, C. Hyland, C. W. MacMinn, A. F. Mertz, L. A. Wilen, Y. Xu, and E. R. Dufresne, *Soft matter* **10**, 4047 (2014).
- [32] J. C. Del Alamo, R. Meili, B. Alonso-Latorre, J. Rodríguez-Rodríguez, A. Aliseda, R. A. Firtel, and J. C. Lasheras, *Proceedings of the National Academy of*

- Sciences **104**, 13343 (2007).
- [33] Y. Xu, W. C. Engl, E. R. Jerison, K. J. Wallenstein, C. Hyland, L. A. Wilen, and E. R. Dufresne, Proceedings of the National Academy of Sciences **107**, 14964 (2010).
 - [34] C. W. Barney, C. Chen, and A. J. Crosby, Soft Matter **17**, 5574 (2021).
 - [35] H. Liang, Z. Cao, Z. Wang, and A. V. Dobrynin, ACS Macro Letters **7**, 116 (2018).
 - [36] H.-J. Butt, R. Berger, W. Steffen, D. Vollmer, and S. A. Weber, Langmuir **34**, 11292 (2018).
 - [37] S. Deguchi, J. Hotta, S. Yokoyama, and T. S. Matsui, Journal of Micromechanics and Microengineering **25**, 097002 (2015).

METHODS

Soft PDMS seeded with quantum dots

First, we sonicate the solution of quantum dots solution (CdSeS/Zns alloyed quantum dots, Sigma Aldrich, #753785) for 5 minutes, and dilute 0.2 mL of this solution in 1.2 mL of toluene in a glass vial with a magnetic stirrer at 350 rpm. Then, we mix 1.25 g of part A and 1.25 g of part B of PDMS precursor (Dowsil™CY52-276 A&B), and very slowly pour the mix into the glass vial. As soon as the mixture looks homogeneous, we put of few drops of it onto a 24 mm × 50 mm coverslip, place it in a spincoater, and spin it at 250 rpm for 60 seconds. We then place the coverslip in a vacuum chamber and apply vacuum for 30 minutes to rapidly evaporate the excess toluene. At last, we put the coverslip in an oven at 40°C for a week to ensure full crosslinking of the PDMS gel.

Confocal imaging

We used a spinning disk confocal system (Yogawa CSU-X1) mounted on an inverted microscope (Nikon, Eclipse Ti2), with a 60x immersion oil objective (MRH02601), with the following settings: 488q laser power 0 and exposure time 1s (to let the immersion oil relax), 560q laser power 100 and exposure time 100ms, and z step size 0.27 μm. To correct for the refractive index difference between the immersion oil $n_{\text{oil}} = 1.518$ and the silicone gel $n_{\text{sil}} = 1.4$ [37], we rescale all z-measurements with the ratio $n_{\text{sil}}/n_{\text{oil}}$.

Polyharmonic interpolation scheme

We estimate the displacement gradients with a polyharmonic spline interpolation scheme (see [22], Chapter 3.8). It amounts to approximating at every position $\mathbf{x} = (x, y, z)$ the displacement field $u(\mathbf{x})$, which can be u_x , u_y , or u_z , as the sum of N radial base spline functions

$$\tilde{u}(\mathbf{x}) = \sum_{i=1}^N w_i \varphi(|\mathbf{x} - \mathbf{x}_i|) + \mathbf{v}^T \cdot \begin{pmatrix} 1 \\ x \\ y \\ z \end{pmatrix}, \quad (1)$$

where \mathbf{x}_i are the positions of a subset of N tracers, w_i are weights to be determined, $\mathbf{v} = (v_0, v_x, v_y, v_z)$ a vector to be determined, and $\varphi(r) = r^3$ the radial base function. We determine the unknowns w_i and \mathbf{v} by solving the linear system

$$\begin{pmatrix} \mathbf{A} & \mathbf{B} \\ \mathbf{B}^T & \mathbf{0} \end{pmatrix} \cdot \begin{pmatrix} \mathbf{w} \\ \mathbf{v} \end{pmatrix} = \begin{pmatrix} \mathbf{u} \\ \mathbf{0} \end{pmatrix}, \quad (2)$$

where $A_{ij} = \varphi(|\mathbf{x}_i - \mathbf{x}_j|)$, $B_{ij} = \delta_{i1} + \delta_{i2}x_j + \delta_{i3}y_j + \delta_{i4}z_j$ with δ the is Kronecker symbol, and u_j is the measured

displacement of tracer j .

Here, we solve the linear system Eq. (2) for each evaluation point \mathbf{x}_n , for which the N tracers are the ones so that $|x_n - x_i| < 10$ microns, $|y_n - y_i| < 10$ microns, and $|z_n - z_i| < 5$ microns. We then estimate the derivatives of the displacement at this evaluation point $\nabla u(\mathbf{x}_n)$ by deriving Eq. (1).

Magnets calibration

We estimate the magnets force-distance relationship with a precision scale. We place the large magnet on the scale, standing on its edge, and gradually approach the vertically-held smaller magnet. We record the weight measured on the scale at various inter-magnet distances d . The resulting force-displacement curve follows an expected dipole-dipole 4th order power law $F \propto d^4$ (Fig. 2b), which we fit to estimate the applied force at any separation distance d .

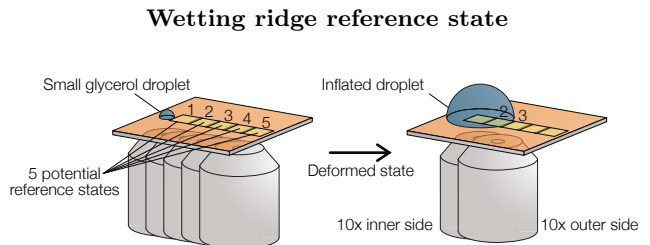


Fig. 4. Sketch of the acquisition of reference and deformed configurations for the surface stretch measurement.

To obtain undeformed, reference states, we proceed as depicted in Fig. 4. First, we deposit a small droplet of glycerol on the soft silicone gel. Second, we acquire 5 overlapping confocal stacks close to the droplet. Third, we add glycerol to the droplet and wait for it reach equilibrium. At last, we image 10 times the deformed states, one on each side of the contact line, corresponding to two of the acquired reference states.

Tangential and normal vectors

We estimate the tangential and normal vectors from the radially collapsed tracer positions in the deformed state (r, z) , which correspond to the surface points of Fig. 3b, and a few built-in Matlab functions. We smooth the vertical positions with the *csaps* function to z_{sm} , compute the radial and vertical gradients (dr, dz_{sm}) with the *gradient* function, and the radial tangent and normal vectors $\mathbf{t}_r = (dr, dz_{\text{sm}})/\sqrt{dr^2 + dz_{\text{sm}}^2}$, $\mathbf{n}_r = (-t_r(2), t_r(1))$. We then project them on the orthoradial line associated to the angular position θ of each tracer to obtain the 3D tangent and normal vectors in the cartesian coordinate system $\mathbf{t} = (t_r(1) \cos \theta, t_r(1) \sin \theta, t_r(2))$, $\mathbf{n} = (n_r(1) \cos \theta, n_r(1) \sin \theta, n_r(2))$.